Available online at www.sciencedirect.com

SCIENCE DIRECT®

Ocean Modelling 8 (2005) 155–173

Ocean Modelling

www.elsevier.com/locate/ocemod

On open boundary conditions for a limited-area coastal model off Oregon. Part 2: response to wind forcing from a regional mesoscale atmospheric model

Jianping Gan *, J.S. Allen, R.M. Samelson

College of Oceanic and Atmospheric Sciences, Oregon State University, Cornvallis, OR 97331-5503, USA

Received 16 September 2003; received in revised form 10 December 2003; accepted 10 December 2003
Available online 31 January 2004

Abstract

This is the second part of a study of open boundary conditions (OBCs) in a limited-area high resolution coastal model off Oregon. In this paper, the OBCs developed in Part 1 [Ocean Modeling, 2005] are further evaluated by an application in which the coastal ocean model is forced with time- and space-dependent wind fields from a regional mesoscale atmospheric model [Journal of Geophysical Research—Oceans 107 (2002)]. The response during summer 1999 of the wind-driven upwelling flow field over the variable shelf bottom topography off Oregon coast is described. Satisfactory performance of the model and of the OBCs in this experiment with complex spatially and temporally varying atmospheric forcing is indicated by the production of physically reasonable fields in the ocean variables and by favorable model/data comparisons. Additional experiments forced by realistic, time-variable, but spatially uniform winds are included to allow a direct comparison of solutions obtained with OBCs and with cyclic boundary condition (CBCs). The general similarity of the results in these two cases provides additional support for the effectiveness of the OBCs in integrating the outer fluxes into, and radiating coastal trapped waves and advective disturbances out of, the computational domain.

Keywords: Open boundary conditions; Modeling; Coastal ocean circulation

* Corresponding author. Present address: Department of Mathematics and Atmospheric, Marine and Coastal Environment (AMCE) Program, Hong Kong University of Science and Technology, Kowloon, Hong Kong.
E-mail address: magan@ust.hk (J. Gan).

1463-5003/$ - see front matter © 2004 Elsevier Ltd. All rights reserved.
doi:10.1016/j.ocemod.2003.12.007

1. Introduction

This is the second part of a study of open boundary conditions (OBCs) in a limited area high resolution coastal ocean model off Oregon. In Part 1, the OBCs are formulated and evaluated in numerical experiments utilizing idealized wind forcing. The objective of this paper is to continue the study from Part 1 by showing the effectiveness of the developed OBCs in providing meaningful model solutions in a situation where realistic wind stress forcing with strong spatial and temporal variability is utilized. As described in Part 1, the OBCs are different for inflow and outflow regimes. The complex field of time- and space-dependent wind stress in the Oregon coastal zone, which forces corresponding complexities in the shelf flow response, provides additional challenges for the OBCs since they have to cope with rapid temporal and spatial changes in the flow regime near the open boundaries.

Over the continental shelf off Oregon during summer, prevailing southward winds produce strong upwelling and an associated southward coastal jet. Time and space variability of the three-dimensional upwelling flow fields and the associated hydrographic regimes are related to variability in the wind stress forcing and to the interactions of the wind-forced currents with the shelf topography. Strong spatial variability in the wind field along the Oregon coast may lead to a corresponding spatial variability in the upwelling flow fields. Fig. 1 shows a 60-day average (June

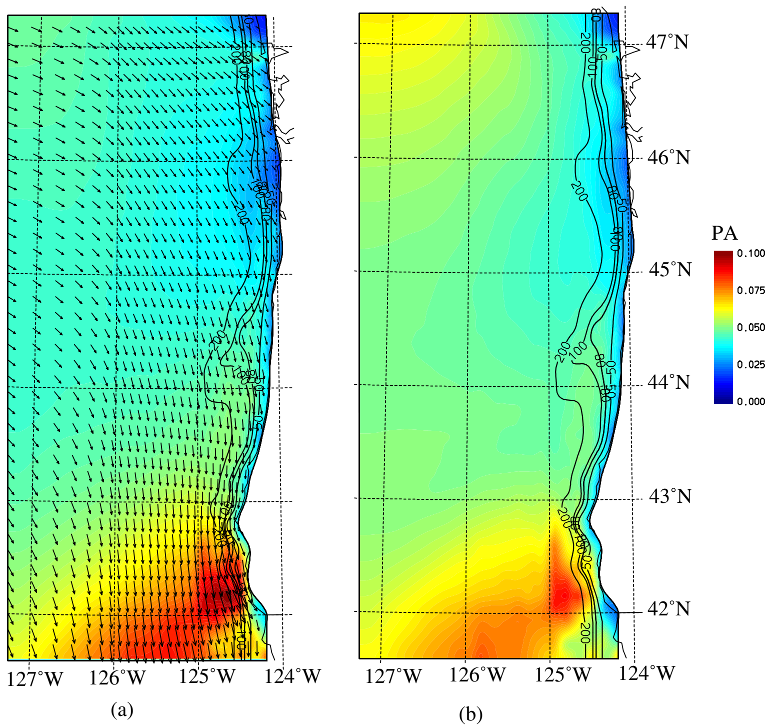

Fig. 1. Time mean wind stress vectors and magnitude (Pa; color); (b) standard deviations of the vector amplitudes (Pa) for the period from 16 June to 14 August 1999 from a regional mesoscale atmospheric model (Samelson et al., 2002).

15–August 15, 1999) of wind stress vectors, wind stress magnitude and the wind stress standard deviation (*std*) obtained from a regional mesoscale atmospheric model (Samelson et al., 2002). Mean south-eastward and southward upwelling favorable wind stress is found in the northern and the southern regions off the Oregon coast, respectively, during this period. Wind stress magnitude gradually increases by a factor of 3–4 toward the south with a strong intensification south of Cape Blanco (42.8°N). A similar pattern of spatial variability is also found in the field of wind stress *std*. Large alongshore variability in wind stress should be expected to change the intensity of the coastal circulation, both locally and remotely through the propagation of coastal trapped waves (CTWs).

The outline of this paper is as follows. The model and its implementation are briefly described in Section 2. The model solutions obtained using wind forcing fields for the Oregon coastal zone from a regional mesoscale atmospheric model are presented in Section 3. Comparisons of model results with observations are given in Section 4. Further evaluations of the OBCs are presented in Section 5 by comparing model solutions using OBCs with those obtained using cyclic boundary conditions (CBCs) in experiments forced with realistic, time-variable, but spatially uniform winds. A summary is given in Section 6.

2. The ocean model

Details about the ocean model and its implementation for the Oregon coast have been given in Part 1. Briefly, the model is the Princeton Ocean Model (POM) (Blumberg and Mellor, 1987) for three-dimensional, time-dependent, oceanographic flows governed by the hydrostatic primitive equations. The model domain extends alongshore 634 km from 41.7°N to about 47.3°N and offshore 250 km, with the coastline boundary fitted by a curvilinear coordinate (Fig. 2). The alongshore coordinate y is aligned approximately north–south with the across-shore coordinate x aligned east–west. The velocity components in the (x, y) directions are (u, v). In order to include meaningful comparable calculations using CBCs for the evaluation of the OBCs, regions with a straight coastline of alongshore extent 10 km north 47°N and 33 km south of 42°N are utilized. The shelf and slope topography is gradually adjusted so that it agrees at the north and south boundaries.

The model is forced with wind stress and atmospheric heat flux from 1 June to August 14 1999. The wind stress forcing is obtained from a regional atmospheric simulation (Samelson et al., 2002) using the University of Oklahoma Advanced Regional Prediction System (ARPS) mesoscale model (Xue et al., 1995). The atmospheric model has an outer 36 km nest and an inner 12 km nest, both centered on 44.7°N 124°W (Newport, Oregon). The inner 12 km domain extends approximately from 41.6°N to 47.8°N and offshore past 128°W. The spatial and the temporal variability in the solutions from the ARPS model were assessed in Samelson et al. (2002) by comparison with time-dependent fields obtained from the QuickSCAT scatterometer. The scatterometer measurements were only available from 21 July to 28 August, but the limited comparisons were generally favorable. Surface wind measurements along the Oregon and northern California coast, used here for comparison with the atmospheric model, are obtained from NOAA buoys located at 46.12°N, 46.6°N, 41.85°N and a land-based NOAA surface meteorological (CMAN) station at

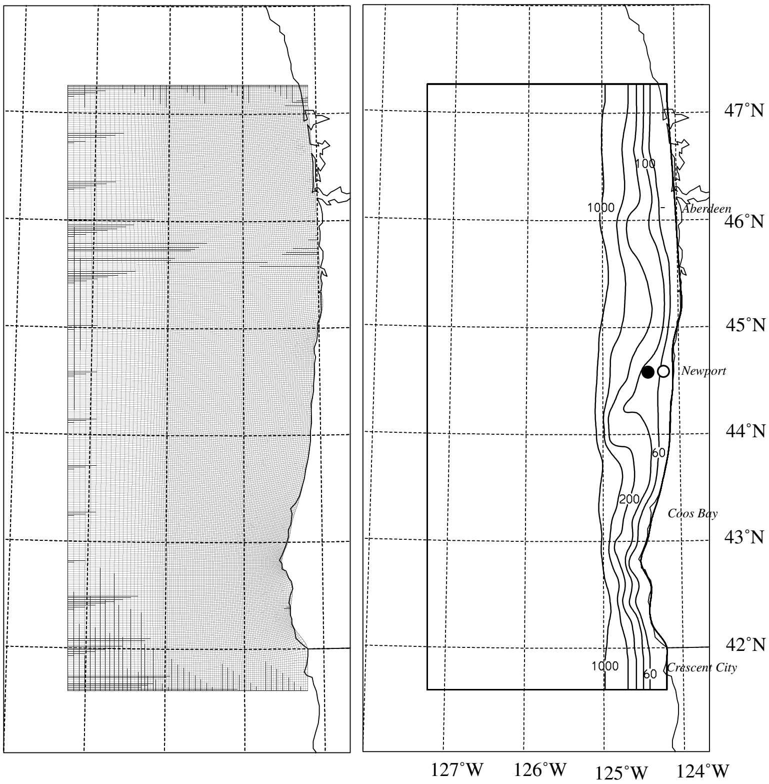

Fig. 2. Model curvilinear grid and bathymetry with the 60, 100, 200, 500 and 1000 m isobaths shown. The horizontal grid spacing ranges from 1.5 km near the coast to 6 km offshore with 45 vertical levels. The grid extends about 633 km alongshore and 250 km across-shore and contains three open boundaries. The open circle is the location of the inshore mooring (50 m) and the solid circle is the location of the midshelf mooring (80 m) and the meteorological buoy.

43.34°N. The measured winds are corrected to 10 m assuming neutral stability and the wind stress is calculated following Large and Pond (1980).

Fig. 3 shows time series of the wind stress from the ARPS model in the 12 km domain and from wind measurements at the stations along the Oregon and California coast. Overall, the wind stress values obtained from the model represent those found from the observations well. Larger deviations between the model solutions and the wind measurements, especially in the east–west component, are found at the southern station (41.85°N) near Crescent City. During June through August 1999, the winds are predominantly southward, i.e., upwelling-favorable, with fluctuations on a several-day time scale. There are a few brief northward (downwelling) events. The strongest upwelling event occurred on 12–14 July, with the largest magnitude southward stress increasing from 0.1 Pa at the northern station Aberdeen (46.12°N) to 0.25 Pa at the southern station Crescent City (41.85°N). The relative magnitudes of these time series are consistent with the spatial structure of the wind stress field in Fig. 1, which shows that the mean alongshore stress increases southward along the coast by a factor of more than four during the study period.

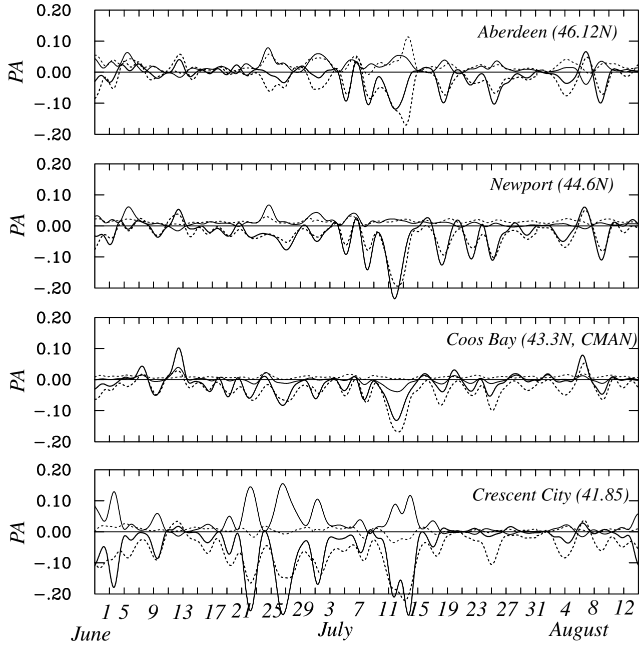

Fig. 3. Time series of wind stress from NDBC buoys off Aberdeen (46.12°N), Newport (44.6°N), Crescent City (41.85°N) and from a CMAN station off Coos Bay (43.3°N). Wind stress values obtained from the atmospheric model are also shown as dashed lines. Thick and thin lines are for north–south and east–west components, respectively.

The wind stress field applied to the ocean model is calculated following Large and Pond (1980) from hourly atmospheric model winds and interpolated to the ocean model grid. The time series of wind stress at each model grid point is then filtered with a 36 h low-pass filter. In the experiments in Section 5 that are forced with spatially uniform winds, time series of winds from the NOAA buoy off Newport (44.6°N) (Fig. 3) are used to calculate a wind stress that is applied uniformly to the entire model domain. In all cases, surface heat flux is obtained from bulk aerodynamic formulae as described in Gan and Allen (2002) using meteorological observations from an OSU meteorological buoy off Newport (44.6°N).

The ocean model is initialized with zero velocities and with horizontally uniform temperature and salinity profiles obtained from climatological values at a location 25 nautical miles off Newport. The simulation is started on June 1 and forced for 75 days. The first 15 days are regarded as a spin-up period, with the following 60 day period used for analysis.

The OBCs applied here are those described in Part 1 (Gan and Allen, 2005). They are based on a separation of the solution at the boundary into global and local parts. The local solution is obtained from a simultaneous calculation using a local time-dependent two-dimensional (variations across-shelf and with depth) submodel at both the northern and southern boundaries. The global part of solution is used to determine the character of the boundary solution with regard to propagation direction of disturbances, based on an Orlanski (1976) type radiation condition. For outflow, the global part of the solution is radiated out of the domain. For inflow, the local solution is imposed with a relaxation time scale λ. A value of $\lambda = 4$ days, which is larger than the values used in Part 1, was found to be necessary here to handle smoothly the effects of the higher time variability in the wind forcing. The time step used in the model integration is 140 s for the internal mode and 140/30 s for the external mode.

In Sections 3 and 4 we discuss the results of the experiment forced with spatially variable wind stress obtained from the ARPS regional mesoscale atmospheric model. We designate this experiment as case 1.

3. Mean fields

3.1. Mean circulation

Time mean oceanographic fields during the 60-day study period contain the averaged responses of upwelling, downwelling and relaxation. The mean fields, however, are dominated by upwelling features due to the mean upwelling-favorable wind stress (Figs. 1 and 3). Time mean surface elevation η and depth-averaged velocity fields (Fig. 4) show the general nature of the upwelling circulation off the Oregon coast.

The mean flow field near the coast is dominated by a southward coastal jet associated with upwelling. Particular topographic features associated with Heceta Bank (44.2°N) and with Cape

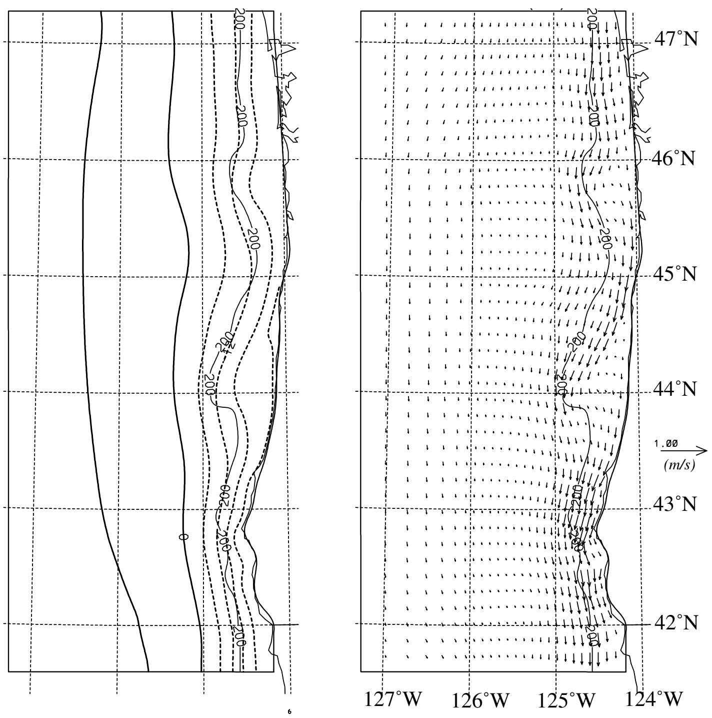

Fig. 4. Time mean surface elevation (contour interval: 6 cm) and mean depth-averaged velocity vectors (m s^{-1}) for the experiment forced by spatially variable winds from a regional mesoscale atmospheric model (case 1).

Blanco (42.8°N) exert a major influence on the mean shelf circulation pattern. The shallowing of the shelf bottom topography over Heceta Bank (44.2°N) results in an offshore veering of the coastal jet at this location, with a region of northward recirculation formed on the inshore side of the Bank. A corresponding response is shown in the η field which decreases toward the coast, reflecting a geostrophic balance of the alongshore current. A northward/southward pressure gradient force is located on the southern/northern edges of the bank as implied by the values of $\partial\eta/\partial y$ that can be inferred from the η field in Fig. 4. A tendency for the coastal jet to separate from the coast south of Cape Blanco (42.8°N) is also evident. Intensification of the southward velocity v, with a corresponding large magnitude of $\partial\eta/\partial x$, is found south of the Cape Blanco due to the strengthening of local wind stress and possibly the narrowing of the shelf in that location. The smooth behavior of the mean η and depth-averaged velocity fields at the northern boundary (NB) and at the southern boundary (SB) indicates that flow disturbances are generally able to propagate northward out of the domain as coastal trapped waves (CTWs) at the NB and likewise able to advect with the alongshore current southward out of the domain at the SB.

The mean surface velocity and the associated *std* fields are shown in Fig. 5. Similar to the depth-averaged flow field, the surface circulation is dominated by the coastal jet which is deflected offshore over Heceta Bank. The mean surface velocity field shows less direct influence of shelf topographic variations than the depth-averaged velocity fields, with no recirculation evident over the Heceta Bank. Relatively high values of the surface velocity *std* are found along the jet core on

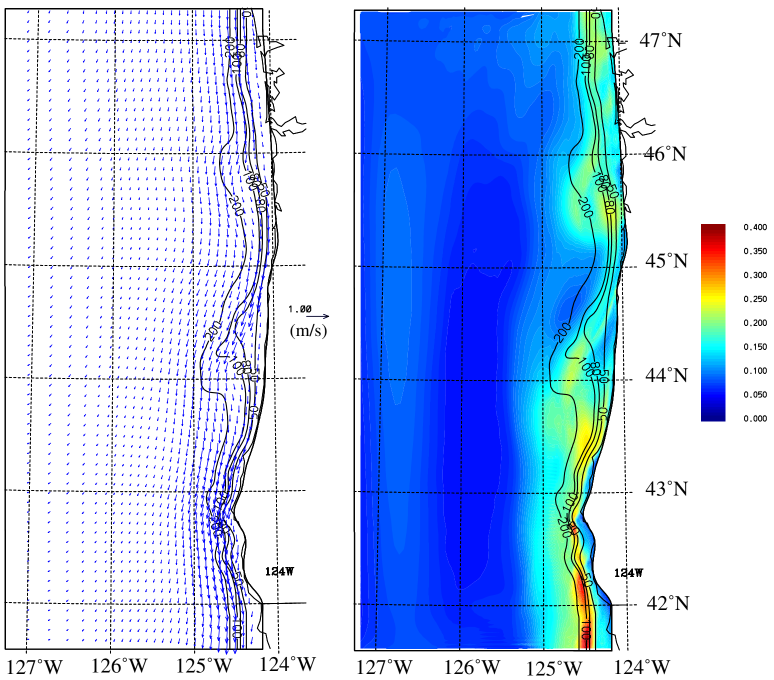

Fig. 5. Time mean surface velocity vectors ($m\,s^{-1}$) and standard deviation of the vector amplitudes (color contours) for the experiment forced by spatially variable winds from a regional mesoscale atmospheric model (case 1).

the shelf both over and south of Heceta Bank and south of Cape Blanco, indicating strong variability in the flow due to interactions between the wind-forced currents and the Bank and reflecting large wind stress variability in the southern part of the domain. Again, the smooth behavior of both the mean and *std* field of the surface velocity at the NB and SB indicates that the OBCs do not produce spurious fluctuations and that interior disturbances are effectively radiated as CTWs, or advected with the alongshore currents, out of the domain. At the same time, inward advective fluxes appear to be maintained satisfactorily.

3.2. Mean density and vorticity fields

High mean surface potential density is found near shore along the coast (Fig. 6) as a result of upwelling. Topographic interactions at Heceta Bank and the much stronger winds in the southern part of the domain contribute to the strengthening of upwelling in these locations. The ratio of local mean surface vorticity to the Coriolis parameter f, a measure of the magnitude of the local

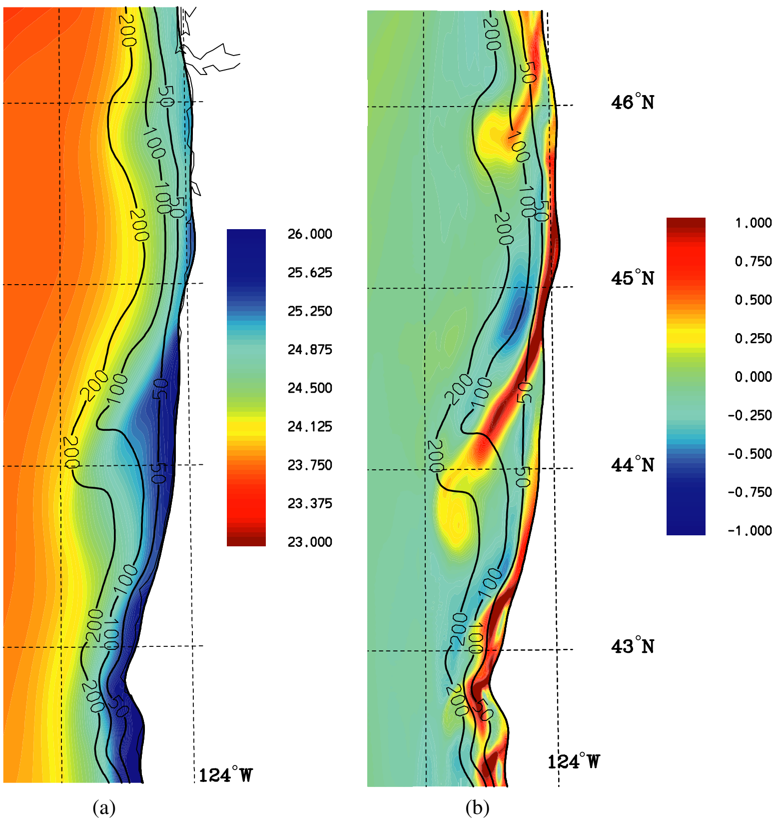

Fig. 6. (a) Time mean surface σ_θ (kg m^{-3}), (b) surface vorticity divided by Coriolis parameter for the experiment forced with spatially variable winds from a regional mesoscale atmospheric model (case 1).

Rossby number, has relatively large (order one) values on the inshore side of the coastal jet (Fig. 6b). The offshore deflection of the jet over Heceta Bank (44.2°N) and the general increase of the inshore vorticity field around Cape Blanco (42.8°N) are evident.

3.3. Mean *v* across-shore sections

To help obtain a three-dimensional picture of the mean alongshore velocity field and its variability, we plot in Fig. 7 the time mean alongshore velocities *v* at across-shore sections at 45°N, off Newport (44.6°N), and in the vicinity of Heceta Bank (44.2°N). The core of the mean

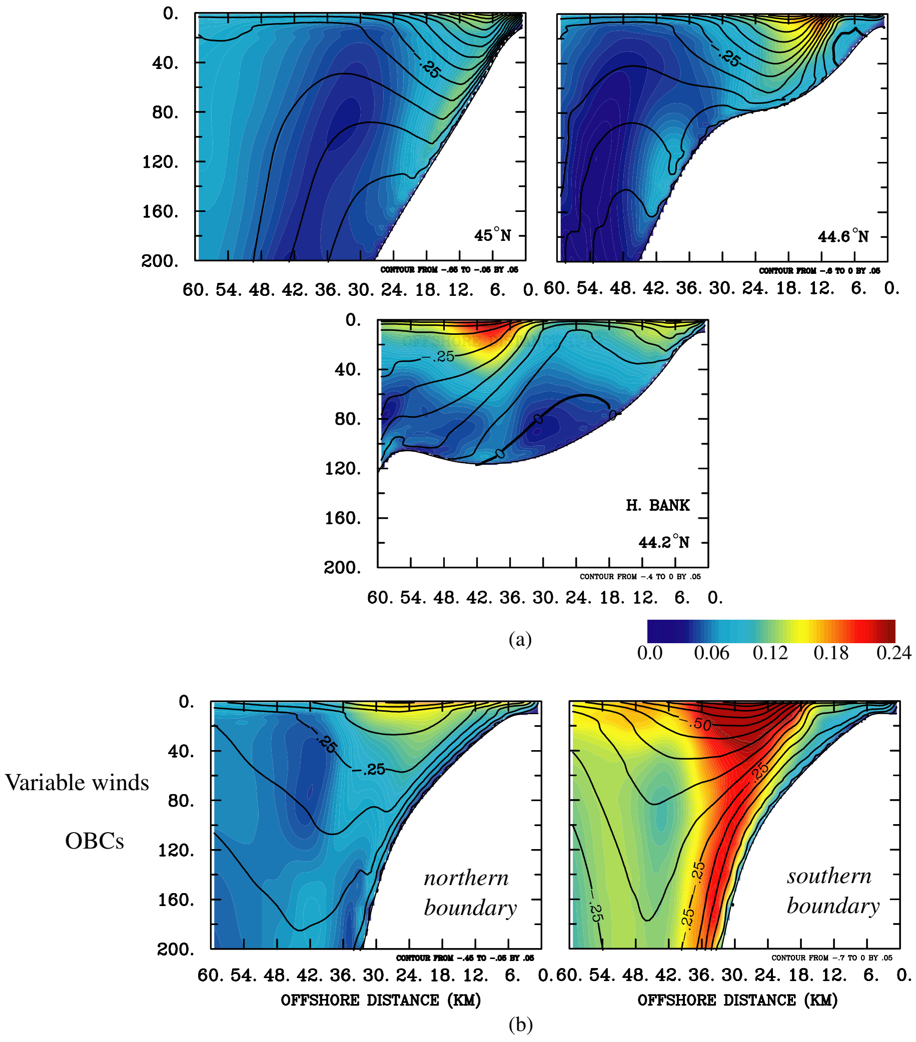

Fig. 7. Across-shore sections of time mean alongshore velocity (m s^{-1}) (black contours) and the corresponding standard deviation (color contours) off 45°N, 44.6°N and 44.2°N (a) and at the northern and southern boundaries (b) for case 1. The contour intervals are 0.05 m s^{-1}.

alongshore jet shifts offshore from north to south in these sections, with increased flow variability evident to the south over Heceta Bank. Mean northward velocities are found in the lower part of the water column near the coast at Newport and at mid-shelf over Heceta Bank. Combined with the southward velocities in the jet farther offshore, this structure reflects the existence of depth-dependent cyclonic recirculation in this region as evident also in the mean depth-averaged velocity fields (Fig. 4). Also visible in the section at Heceta Bank (44.2°N) is the presence of an additional weaker southward jet within 12 km of the coast.

Similar plots of across-shore sections of v at the NB and SB (Fig. 7) show smooth and physically reasonable flow fields. Much stronger velocities, with magnitudes up to about 0.8 $\mathrm{m\,s^{-1}}$ are found at the SB, compared with maximum magnitudes of about 0.45 $\mathrm{m\,s^{-1}}$ at the NB. The standard deviations of v are likewise considerably larger at the SB. The larger magnitude mean and fluctuating values at v in the south presumably reflect to a large extent the substantially stronger wind stress in this region.

4. Comparisons with mooring data

The usefulness of the OBCs with time- and space-dependent wind forcing is further evaluated in this section by a comparison of the model solutions with available measurements.

Two current meter moorings, one at an inshore (50 m) and one at a mid-shelf (80 m) location, were deployed along a line on the continental shelf west of Newport (44.6°N) in summer 1999 (Fig. 2). Time series of the model and the observed alongshore velocities from different measurement depths at the inshore and at the mid-shelf mooring locations are shown in Fig. 8. Both model and observed velocities have been filtered by averaging over an inertial period. The alongshore directions are defined here as the individual directions of the major principal axes of each velocity vector time series. Corresponding time series for the potential temperature are shown in Fig. 9. Correlation coefficients (CCs) and the root mean square errors (rmse) between the corresponding observations and model variables are also given in Figs. 8 and 9. The currents near the surface and at depth from both moorings vary in response to the wind stress (Fig. 3). Model and observed currents are well correlated, with larger correlation coefficients (CC $\geqslant$ 0.7) found at the inshore mooring (Fig. 8). At the mid-shelf mooring, the CC values are smaller at 20 m, but increase with depth. The model velocities at the location of the mid-depth mooring, however, are stronger southward than the observed velocities after July 31. Overall, a consideration of the CCs and rmse values indicated in Figs. 8 and 9, shows better performance of the model currents at the inshore location compared to that at the midshelf. Similar across-shelf spatial variations in the correlation coefficients between model and observed alongshore currents with higher values inshore have been found in other simulations of wind-forced shelf currents with CBCs (e.g., Gan and Allen, 2002; Oke et al., 2002).

The near surface temperature from 4m depth at the location of the inshore mooring (Fig. 9) varies in response to the alongshore wind stress. Surface cooling occurs between July 12 and 14 as a result of the intensification of upwelling in response to the increase in southward winds. A strong surface warming occurs after July 31 associated with the northward currents near the coast that develop after the relaxation of upwelling favorable winds. The variation of temperature measurements in the deeper water is relatively small. The CC values for the time series of tem-

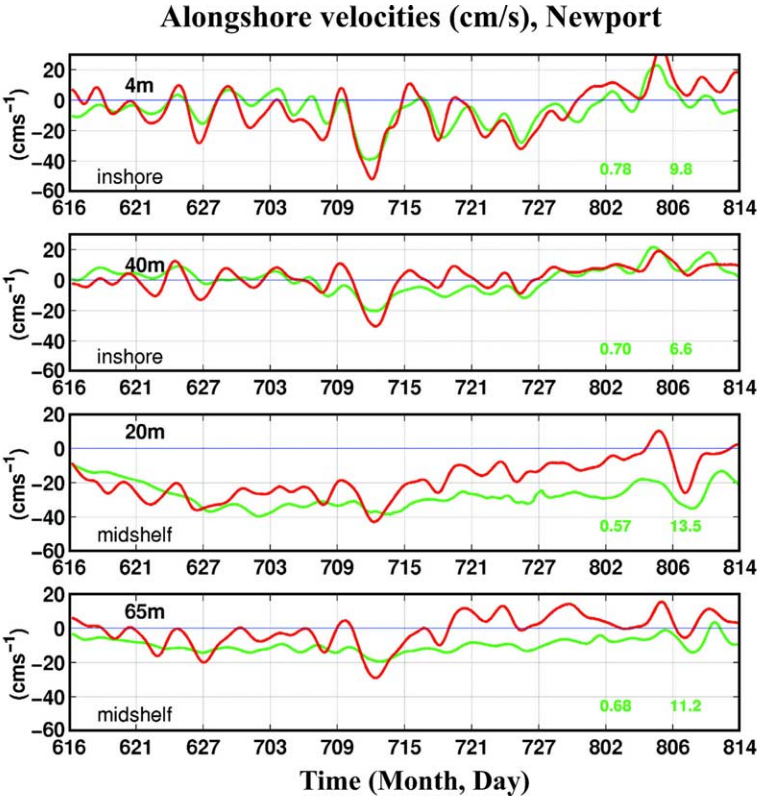

Fig. 8. Time series of observed (red lines) and modeled (green lines, case 1) inertially-averaged alongshore velocities at 4 m and 40 m depths at the inshore mooring (water depth: 50 m) and at 20 m and 65 m depths at the midshelf mooring (water depth 80 m). Correlation coefficients and root mean square error (rmse) between the corresponding observed and modeled velocities are noted. The alongshore directions here are defined as the individual directions of the major principal axes of each vector time series.

perature are larger (0.72) near the surface at the inshore mooring and decrease with depth and at the mid-shelf mooring. The general agreement of the range of temperature values at depth in the model and observations suggests that the model solutions represent a realistic thermal field over the shelf.

5. OBCs vs. CBCs

In a coastal model with CBCs and no alongshore coastal boundaries the numerical problem is comparatively well defined. As mentioned in Part 1, the errors caused by CBCs which assume periodic coastal topography and forcing can be reasonably small for a limited time integration (e.g. Gan and Allen, 2002; Oke et al., 2002). The solutions obtained from a coastal model with CBCs can thus be usefully treated as benchmark results for comparison with those obtained with OBCs. The use of CBCs, however, requires that the wind stress forcing have the same values at the

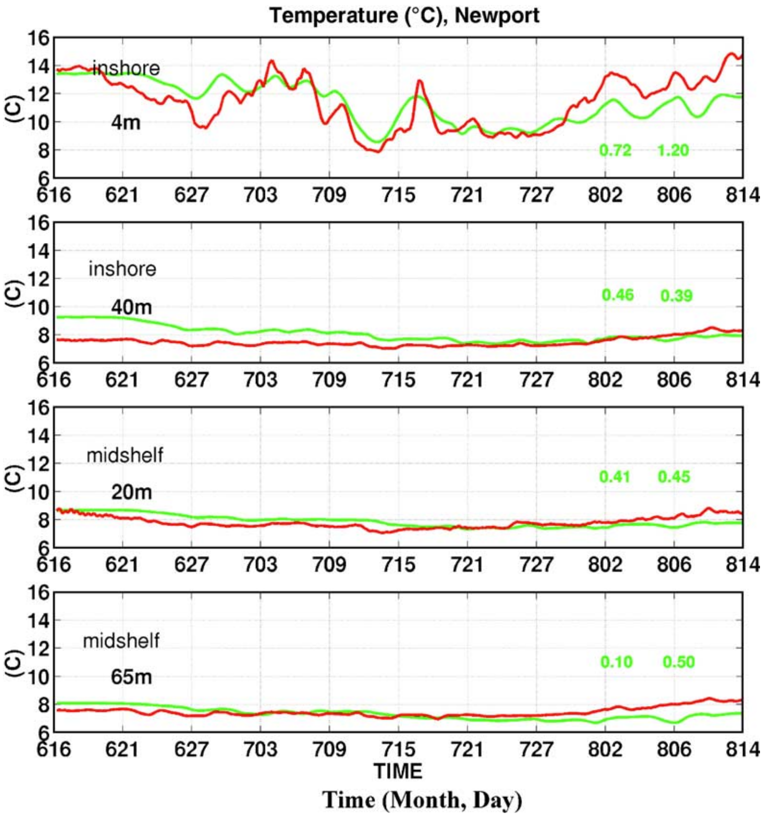

Fig. 9. Time series of observed (red lines) and modeled (green lines, case 1) inertially-averaged temperature at 4 m and 40 m depths at the inshore mooring (water depth 50 m) and at 20 m and 65 m depths at the midshelf mooring (water depth 80 m). Correlation coefficients and rmse between the corresponding observed and modeled temperature values are noted.

NB and SB. Consequently, to make a sensible comparison between solutions obtained using OBCs and CBCs with the same forcing, spatially uniform wind stress is used, but with realistic temporal variability. In these experiments, the wind stress is obtained from the buoy winds measured at Newport (44.6°N) (Fig. 3). Note that the winds near Newport are weaker than in the southern part of the domain.

The evolution of volume-averaged kinetic energy (KE) and volume-averaged temperature (TA) for the experiments forced with spatially variable winds from the mesoscale atmospheric model (case 1), with spatially uniform winds using OBCs (case 2), and with spatially uniform winds using CBCs (case 3) is shown in Fig. 10. Similarities between the results from case 2 and case 3 are expected if the OBCs perform reasonably well. The results in Fig. 10 show the differences in KE and TA for case 2 with OBCs and case 3 with CBCs were not significant. For case 1 with variable winds, KE is generally larger and TA is 0.1–0.2 °C lower than both cases 2 and 3. This is because of the presence of larger wind stress to the south in the spatially variable wind case (Fig. 1). The dynamics involved in creating the KE and TA differences in case 1 and case 2 are discussed further

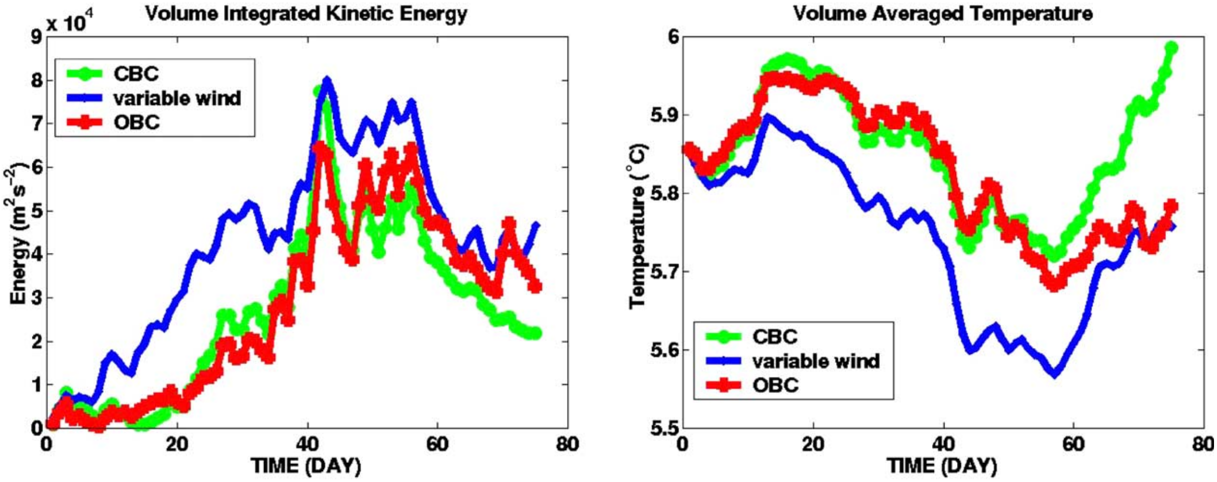

Fig. 10. Time series of volume-averaged kinetic energy (KE) and temperature (TA) for experiment forced with spatially variable winds (case 1) and for the experiments with spatially uniform winds using both OBCs (case 2) and CBCs (case 3).

below in connection with a comparison of differences in the time mean surface potential density and vorticity fields.

The similarities between case 2 and case 3 results can also be seen from the mean surface elevation fields and mean depth-averaged velocity fields in Fig. 11. In both cases, the −6 cm contour line of η roughly follows the 200 m isobath. Slightly stronger currents inshore of the 200 m isobath are found in case 3 with CBCs as indicated by the fact that the −3 cm contour line in the η field is located farther offshore. The same general characteristics of depth-averaged circulation are shown in both cases, with the coastal jet moving offshore over Heceta Bank accompanied by a weak cyclonic circulation inshore over the Bank.

The values of mean surface potential density from cases 2 and 3 (Fig. 12) are close over the shelf inshore of the 200 m isobath, with slightly higher values found in case 2 with OBCs. Offshore of the 200 m isobath, the solutions with CBCs have lower mean surface potential density. A close correspondence in dynamical characteristics of the flow response to Heceta Bank in cases 2 and 3 is implied by the similarity in the ratios of mean local surface vorticity to Coriolis parameter (Fig. 13).

The across-shore sections of alongshore velocities at the NB and the SB from case 2 with OBCs and case 3 with CBCs are shown in Fig. 14. The v sections at the NB and SB are identical in case 3 with CBCs as they should be and are very similar to the v section at the SB from case 2. The alongshore currents at the NB are weaker in magnitude with OBCs. This feature is consistent with the results found in Part 1 with idealized wind stress and attributed there to the possibility that alongshore pressure gradients in the three-dimensional region can geostrophically balance wind-driven onshore flow beneath the surface Ekman layer. This results in a decreased acceleration of the coastal jet relative to that found in the two-dimensional local solution, or in this case, to that found in the near uniform topography regions near the boundary with CBCs. Away from the open boundaries, the magnitudes and structure of v in the model interior at sections 45°N, Newport (44.6°N) and Heceta Bank (44.2°N) are very similar in cases 2 and 3 (Fig. 15).

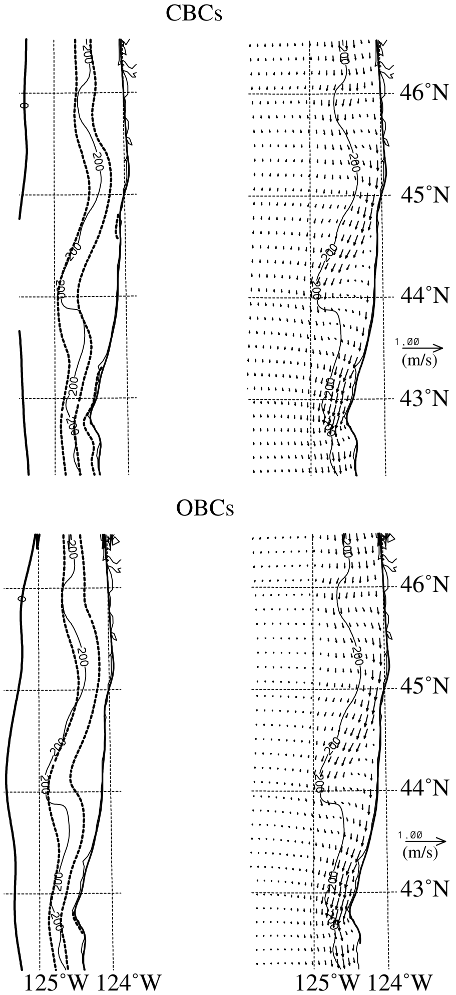

Fig. 11. Time mean surface elevation (cm) and depth-averaged velocity vectors ($m\,s^{-1}$) for the experiments forced with spatially uniform winds using both CBCs (case 3) and OBCs (case 2).

The solution from the experiment forced with spatially variable winds (case 1) shows many differences from the solutions obtained with spatially uniform winds (cases 2 and 3). Higher surface potential density (Fig. 6 vs. 12) and larger local Rossby numbers are found in case 1 (Fig. 6 vs. 13). These features are shown explicitly in Fig. 16 in plots of the difference of the time mean surface potential density and surface vorticity fields for case 1 minus case 2. The difference in density is largest near the coast at the southern boundary and it decreases continuously in the northward direction. This reflects the increased offshore Ekman transport and thus increased upwelling into the surface layer in response to the large wind stress in the south in case 1 with spatially variable winds. The difference vorticity field shows the presence of generally larger positive values in case 1. There is some decrease in magnitude toward the north, but the gradient is considerably smaller than in the difference density field. This behavior is consistent with the

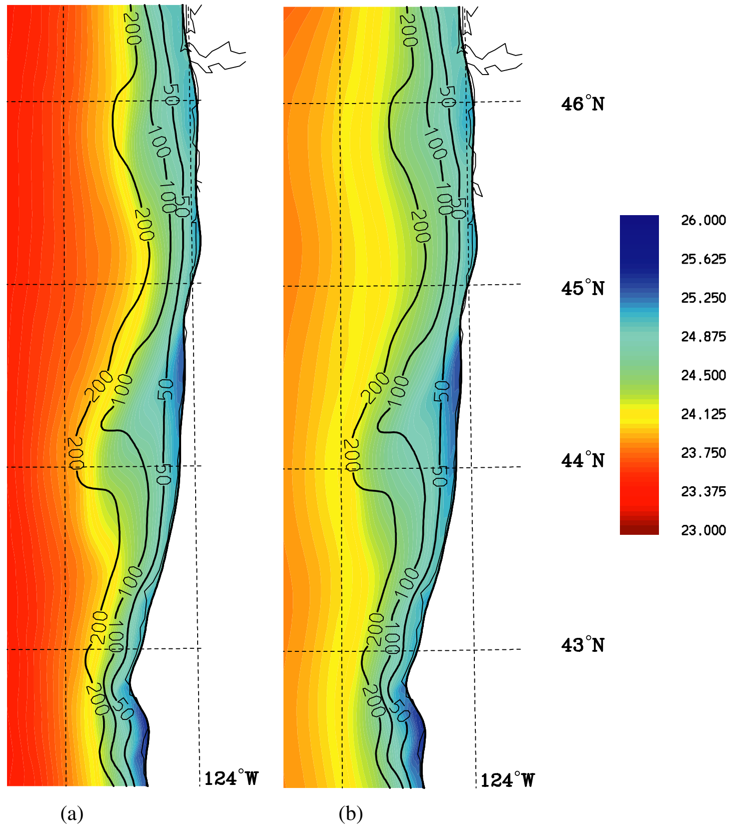

Fig. 12. Time mean surface σ_θ (kg m^{-3}) for the experiments forced with spatially uniform winds using both (a) CBCs (case 3) and (b) OBCs (case 2).

northward propagation by CTWs of disturbances forced by the stronger winds in the south in case 1. As a result, the generally southward alongshore currents are strengthened throughout the domain and, in particular, the positive vorticity on the inshore side at the coastal jet is intensified. The strengthened alongshore currents in the north are accompanied, through the thermal wind balance, by changes in the shelf density field characterized by upward isopycnals near the coast. The net effect of those changes on the time mean surface density, however, is evidently small compared to that due to local wind forcing of offshore Ekman transport and upwelling in the southern region (Fig. 16). The effect of northward energy propagation by CTWs with spatially variable wind forcing was demonstrated in Part 1 (Section 5.1).

In addition, we note that better agreement with observations of alongshore velocity at the inshore and midshelf moorings is found with case 1, i.e., generally higher CCs and lower rmse compared to cases 2 or 3. We add a note of caution here because in this application of the OBCs there is an implicit assumption that the winds to the south of the OB are uniformly the same strength as those on the south boundary of the computational domain. This assumption may lead to an overestimate of the strength of wind-forced fluctuations emanating from the south boundary as CTWs. Nevertheless, the results clearly demonstrate the dynamical importance of spatially

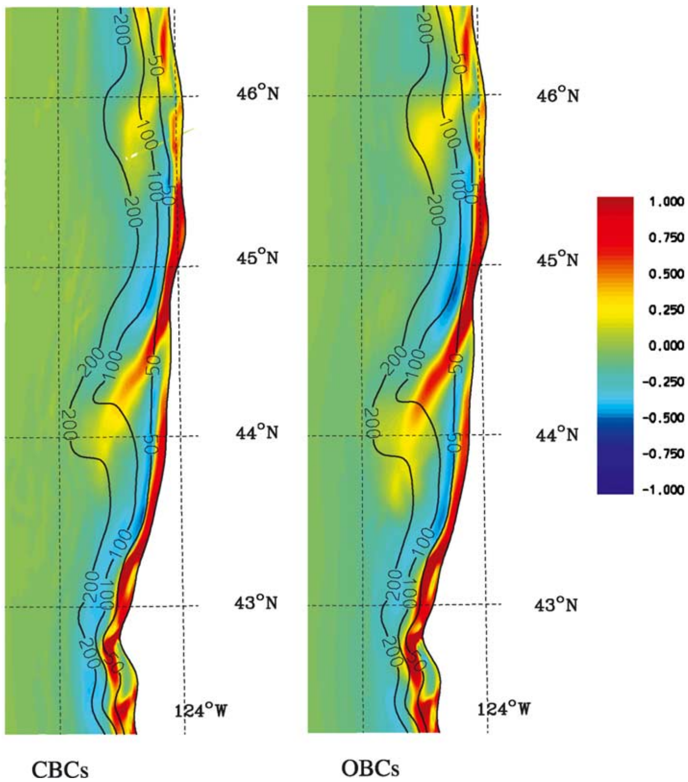

Fig. 13. Time mean surface vorticity divided by the Coriolis parameter f for the experiments forced with spatially uniform winds using both CBCs (case 3) and OBCs (case 2).

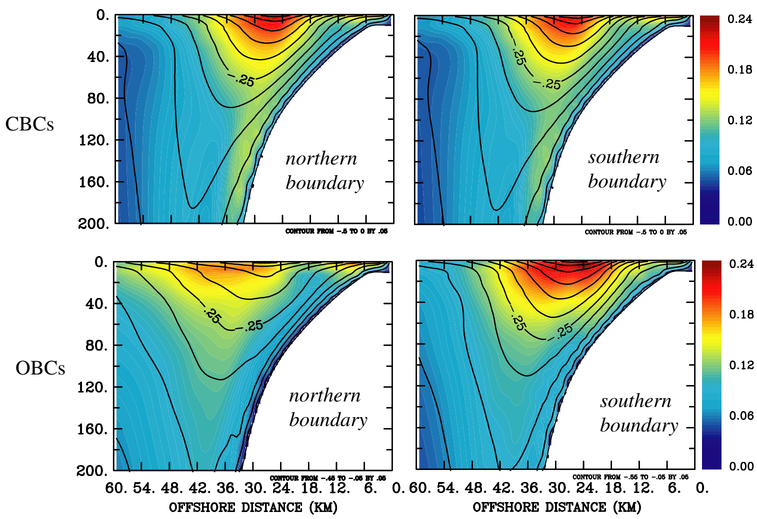

Fig. 14. Across-shore sections of time mean alongshore velocity (m s^{-1}) (black contours) and the corresponding standard deviations (color contours) at the northern and the southern boundaries for the experiments forced with spatially uniform winds using both CBCs (case 3) and OBCs (case 2). The contour intervals are 0.05 m s^{-1}.

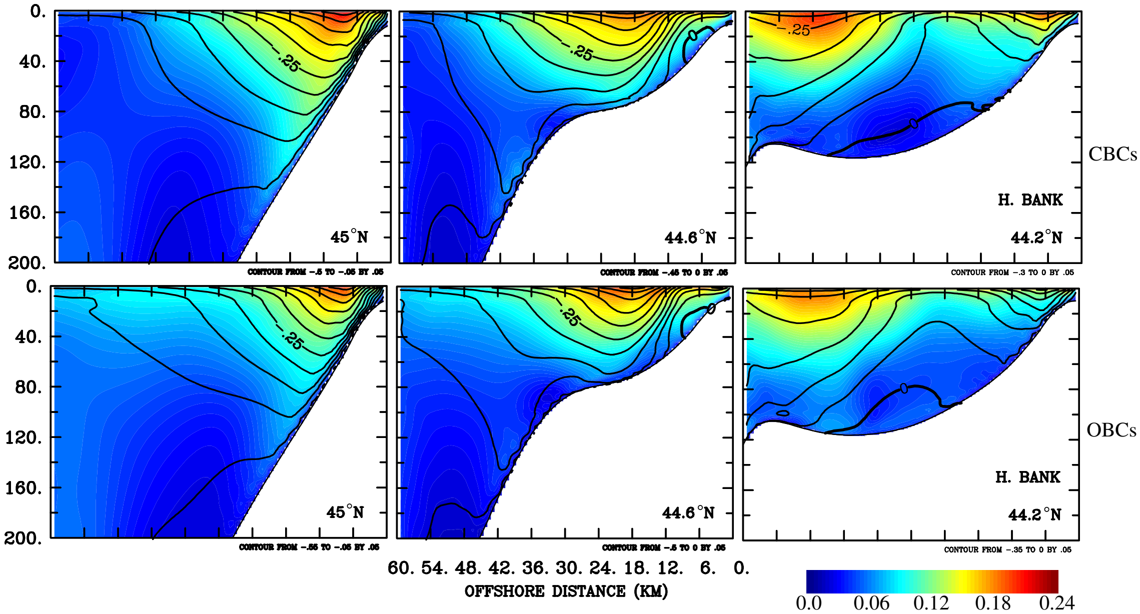

Fig. 15. Across-shore sections of time mean alongshore velocity (m s^{-1}, black contour lines) and the corresponding standard deviations (color contours) off 45°N, 44.6°N and 44.2°N for the experiments forced with spatially uniform winds using both CBCs (case 3) and OBCs (case 2). The contour intervals are −0.05 m s^{-1}.

variable winds on the upwelling circulation over the Oregon continental shelf. These effects will be investigated in more detail in future studies. It should be noted that by obtaining the local solutions at the NB and SB from two-dimensional sub-models in this study, we essentially assume that the winds on the NB and SB are applied everywhere in the regions to the north and south of NB and SB with the same across-shore topography, respectively. Thus, the influence from spatial wind variations outside the current model domain is not included in the model solutions. The model solutions obtained with the current OBCs reflect the wind-forced shelf flow dominated by local flow topography interaction. An improvement is to be pursued by providing the local solution from a regional ocean model in a larger domain using nesting.

6. Summary

As a second part of this study of OBCs for a limited-area coastal model off Oregon, we apply the OBCs developed in Part 1 to an experiment forced with time- and space-dependent wind fields obtained from a regional mesoscale atmospheric model for summer 1999. The model appears to provide a reasonable simulation of the upwelling circulation off the Oregon coast. The OBCs are evidently able to integrate outer fluxes inward during inflow conditions and to radiate CTW or advective disturbances outward during outflow conditions without noticeable distortion of the solutions either at the open boundaries or in the interior of the model domain.

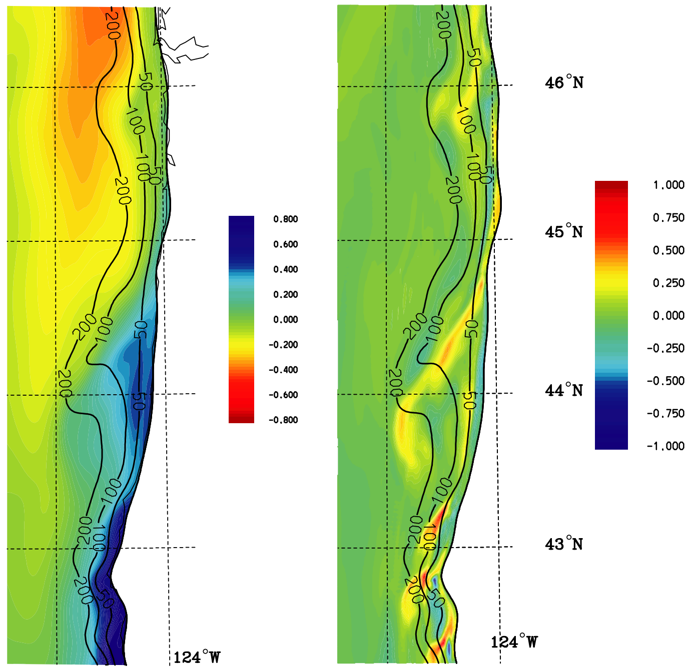

(a) (b)

Fig. 16. Differences of time mean (a) surface σ_θ (kg m^{-3}) and (b) surface vorticity divided by Coriolis parameter between the experiment forced with spatially variable winds from a regional mesoscale atmospheric model (case 1) and the experiment forced with spatially uniform winds using OBCs (case 2).

The solutions are assessed based on model–data comparisons. The model alongshore velocities show good agreement with available measurements over the shelf off Newport (44.6°N). The performance of the OBCs is also evaluated in additional experiments forced with time-dependent, spatially uniform winds by comparison of results obtained with CBCs. The general similarity of the solutions in these two experiments with different boundary conditions provides additional confidence in the performance of the OBCs.

The results of this study also show that realistic spatial variability of the wind field can have significant effects on modeled shelf flow fields. The dynamical implications of spatially variable winds for the Oregon shelf will be addressed in future studies.

Acknowledgements

This research was supported by the National Science Foundation Coastal Ocean Processes (CoOP) program under grant OCE-9907854. We thank two anonymous reviewers for helpful comments. J. Gan is grateful to Hong Kong University of Science and Technology for supports.

References

Blumberg, A.F., Mellor, G.L., 1987. A description of a three-dimensional coastal ocean circulation model. In: Heap, N. (Ed.), Three-Dimensional Coastal Ocean Models, vol. 4. AGU, Washington, DC, p. 208.

Gan, J.P., Allen, J.S., 2002. A modeling study of shelf circulation off northern California in the region of the Coastal Ocean Dynamics Experiment. 2. Simulations and comparisons with observations. J. Geophys. Res.—Oceans 107 (C11), 3184, doi:10.1029/2001JC001190.

Gan, J.P., Allen, J.S., 2005. On open boundary conditions for a limited-area coastal model off Oregon. Part 1. Response to idealized wind forcing. Ocean Modeling, this issue.

Large, W.G., Pond, S., 1980. Open ocean momentum flux measurements in moderate to strong winds. J. Phys. Oceanogr. 11, 324–336.

Oke, P.R., Allen, J.S., Miller, R.N., Egbert, G.D., Austin, J.A., Barth, J.A., Boyd, T.J., Kosro, P.M., Levine, M.D., 2002. A modeling study of the three-dimensional continental shelf circulation off Oregon. I. Model–data comparisons. J. Phys. Oceanogr. 32, 1360–1382.

Orlanski, I., 1976. A simple boundary condition for unbounded hyperbolic flows. J. Comput. Phys. 21, 251–269.

Samelson, R.M., Barbour, P., Barth, J., Bielli, S., Boyd, T., Chelton, D., Kosro, P., Levine, M., Skyllingstad, E., Wilczak, J., 2002. Wind stress forcing of the Oregon coastal ocean during the 1999 upwelling season. J. Geophys. Res.—Oceans 107 (C5), doi:10.1029/2001JC000900.

Xue, M., Droegemeir, K., Wong, V., Shapiro, A., Brewster, L., 1995. ARPS Version 4.0 User's Guide. Cent. for Adv. and Predict. of Storms, Univ. Okla., Norman, Okla, 380 pp.